

Supernovae from Red Supergiants with Extensive Mass Loss

Takashi Moriya^{1,2,3*}, Nozomu Tominaga^{4,1}, Sergei I. Blinnikov^{5,6,7,1},
 Petr V. Baklanov⁵, & Elena I. Sorokina^{6,7}

¹ *Institute for the Physics and Mathematics of the Universe, Todai Institutes for Advanced Study, University of Tokyo, Kashiwanoha 5-1-5, Kashiwa, Chiba 277-8583, Japan*

² *Department of Astronomy, Graduate School of Science, University of Tokyo, 7-3-1 Hongo, Bunkyo-ku, Tokyo 113-0033, Japan*

³ *Research Center for the Early Universe, Graduate School of Science, University of Tokyo, 7-3-1 Hongo, Bunkyo-ku, Tokyo 113-0033, Japan*

⁴ *Department of Physics, Faculty of Science and Engineering, Konan University, 8-9-1 Okamoto, Kobe, Hyogo 658-8501, Japan*

⁵ *Institute for Theoretical and Experimental Physics, Bolshaya Cheremushkinskaya 25, 117218 Moscow, Russia*

⁶ *Sternberg Astronomical Institute, Moscow University, Universitetski pr. 13, 119992 Moscow, Russia*

⁷ *Max-Planck-Institut für Astrophysik, Karl-Schwarzschild-Str. 1, 85741 Garching, Germany*

23 September 2018

ABSTRACT

We calculate multicolor light curves (LCs) of supernovae (SNe) from red supergiants (RSGs) exploded within dense circumstellar medium (CSM). Multicolor LCs are calculated by using a multi-group radiation hydrodynamics code STELLA. If CSM is dense enough, the shock breakout signal is delayed and smeared by CSM and kinetic energy of SN ejecta is efficiently converted to thermal energy which is eventually released as radiation. We find that explosions of RSGs are affected by CSM in early epochs when mass-loss rate just before the explosions is higher than $\sim 10^{-4} M_{\odot} \text{ yr}^{-1}$. Their characteristic features are that the LC has a luminous round peak followed by a flat LC, that multicolor LCs are simultaneously bright in ultraviolet and optical at the peak, and that photospheric velocity is very low at these epochs. We calculate LCs for various CSM conditions and explosion properties, i.e., mass-loss rates, radii of CSM, density slopes of CSM, explosion energies of SN ejecta, and SN progenitors inside, to see their influence on LCs. We compare our model LCs to those of ultraviolet-bright Type IIP SN 2009kf and show that the mass-loss rate of the progenitor of SN 2009kf just before the explosion is likely to be higher than $10^{-4} M_{\odot} \text{ yr}^{-1}$. Combined with the fact that SN 2009kf is likely to be an energetic explosion and has large ^{56}Ni production, which implies that the progenitor of SN 2009kf is a massive RSG, our results indicate that there could be some mechanism to induce extensive mass loss in massive RSGs just before their explosions.

Key words: circumstellar matter – stars: mass-loss – supernovae: general – supernovae: individual (SN 2009kf)

1 INTRODUCTION

What kind of stars becomes which kind of supernovae (SNe)? There still no conclusive answer to this simple question. Looking into the case of core-collapse SNe (CCSNe) which result from death of massive stars, there are several discrepancies between answers from observers and theorists. Observers get information about the progenitors of CCSNe by directly getting images of the SN progenitors by looking into the archival images of the SN site (Smartt 2009, and the references therein) or statistically analysing the number of

SNe appeared (e.g., Smith et al. 2010; Boissier & Prantzos 2009; Arcavi et al. 2010). On the other hand, theorists have been calculating evolution of massive stars for decades to get progenitor models of SNe. Theoretical pictures of single star evolution without rotation are well summarized in Heger et al. (2003).

One of the big discrepancies raised recently between observers and theorists is the zero-age main-sequence (ZAMS) mass range of Type IIP SN progenitors. Type IIP SNe are the most common type of CCSNe which results from explosions of red supergiants (RSGs) with a large amount of hy-

* takashi.moriya@ipmu.jp

drogen¹. Both observers and theorists suggest that the minimum ZAMS mass of Type IIP SN progenitors at solar metallicity is $\sim 8 M_{\odot}$ (Smartt et al. 2009; Heger et al. 2003). Meanwhile, the maximum ZAMS mass of Type IIP SN progenitors from theoretical calculations of solar-metallicity single star evolution is $\sim 25 M_{\odot}$ (Heger et al. 2003, and the references therein) but the observations suggest that the maximum ZAMS mass is $\sim 17 M_{\odot}$ (Smartt et al. 2009).

This big discrepancy partly comes from uncertainties in theoretical models. One of the big uncertainties in modeling stellar evolution is in mass loss. The canonical single star modeling uses empirical mass-loss rates but there are many mechanisms to induce mass loss which are not taken into account in such empirical mass-loss rates. For example, the effect of stellar rotations on mass-loss rates are studied for a long time and it is found that the maximum ZAMS mass of the Type IIP SNe can be reduced by including stellar rotations (Georgy et al. 2009, and the references therein). Mass loss due to the pulsations driven by partial ionization of hydrogen in the envelope of RSGs (e.g., Yoon & Cantiello 2010; Heger et al. 1997; Li & Gong 1994) is another candidate for the missing mass-loss mechanism. This kind of mass loss due to pulsations occurs in a dynamical timescale and it is usually not followed by stellar evolution codes. Yoon & Cantiello (2010) analyse the dynamical instabilities of RSGs and show that RSGs whose ZAMS mass is above $\sim 17 M_{\odot}$ suffer from this instability and their mass-loss rate can potentially be as high as $\sim 10^{-2} M_{\odot} \text{ yr}^{-1}$. Such existence of extensive mass loss in massive RSGs may not allow massive RSGs to explode as Type IIP SNe and could reduce the maximum ZAMS mass of Type IIP SN progenitors. It is worth noting that the minimum ZAMS mass to cause the pulsations is the same as the maximum ZAMS mass of Type IIP SN progenitors indicated by observations ($\sim 17 M_{\odot}$). Nuclear flashes which may occur during the evolution of massive stars can also be a candidate for the driving force of such extensive mass loss (Weaver & Woosley 1979; Dessart, Livne, & Waldman 2010). If such extensive mass loss takes place commonly during the evolution of massive stars, theoretical predictions for the maximum ZAMS mass of Type IIP SN progenitors can be as low as what observations imply. The existence of binary systems is also suggested to be account for this problem (e.g., Smith et al. 2010).

There are also observed potential Type IIP SN progenitors (RSGs) which are losing their mass with very high mass-loss rates. For example, a RSG VY Canis Majoris is estimated to be losing its mass with the rate $1 - 2 \times 10^{-3} M_{\odot} \text{ yr}^{-1}$ from the direct observations of circumstellar medium (CSM) around it (Smith, Hinkle, & Ryde 2009). Observations of dusts around another RSG IRAS05280-6910 also indicate the extensive mass loss ($\sim 10^{-3} M_{\odot} \text{ yr}^{-1}$) of the RSG (Boyer et al. 2010). Some Type IIP SNe are reported to show the possible effect of dense CSM in their LCs and spectra. A representative example of this kind is ultraviolet(UV)-bright Type IIP SN 2009kf (Botticella et al. 2010). SN 2009kf was bright in UV for ~ 10 days during its early epochs as well as in optical. Later, the LC transformed to that of a Type IIP SN and the spectra taken at later epochs are classified as Type IIP. The fact that SN

2009kf was bright in UV and optical at the same time makes it difficult to explain SN 2009kf without CSM interaction. This is because usual Type IIP SNe cool adiabatically in their early epochs and they become optically bright after UV brightness gets weaker. Utrobin, Chugai, & Botticella (2010) show a LC model of SN 2009kf without CSM interaction but the required explosion energy is found to be very high (2.2×10^{52} erg). Another Type IIP SN 2007od (Andrews et al. 2010) had late phase spectra similar to those of Type IIn SN 1998S, which are considered to result from CSM interaction (Pozzo et al. 2004). Also, SN 2007od showed the possibility of the existence of light echos in its LC and it may indicate the existence of CSM around the progenitor (Andrews et al. 2010).

The existence of dense CSM around SN progenitors at the time of their explosions can affect their LCs. If a SN explosion occur in dense CSM, the shock breakout signal from the SN diffuse out in CSM. In addition, the SN ejecta is decelerated by the dense CSM. Thus, the kinetic energy of the ejecta is efficiently converted to the thermal energy which is eventually released as radiation energy. This extra heat source makes the SN brighter than usual SNe. So far, SNe powered by the interactions of SN ejecta and dense CSM are mainly modeled in the context of Type IIn SNe showing narrow emission lines which are a clear evidence of the interaction of SN ejecta and CSM (e.g., Chugai et al. 2004; Woosley, Blinnikov, & Heger 2007; Dessart et al. 2009; van Marle et al. 2010; Metzger 2010). Here, given the possibilities that RSGs can have enhanced mass-loss rates and that dense CSM can exist around RSGs at the time of the explosions, we investigate the effect of dense CSM on LCs from SNe of RSGs with dense CSM. Some works (e.g., Falk & Arnett 1973, 1977) have already done with the similar conditions but, in this paper, we model them more systematically and with better treatments of physics. To model the LCs powered by the shock interactions, we have to follow radiation hydrodynamics because the energy source of the radiation is a hydrodynamical shock wave. Thus, we adopt a multi-group radiation hydrodynamics code **STELLA** developed by Blinnikov & Bartunov (1993); Blinnikov et al. (1998, 2006), which has been applied for modeling LCs powered by shock interactions (e.g., Chugai et al. 2004; Woosley, Blinnikov, & Heger 2007; Blinnikov & Sorokina 2010).

This paper is composed of five sections. We first briefly summarize **STELLA** and the pre-SN models we adopt in Section 2. Synthesized LCs with various CSM conditions are shown in Section 3. In Section 4, we compare our models with the LCs of SN 2009kf and show that the LCs powered by the interaction of SN ejecta and dense CSM is actually consistent with the LCs of SN 2009kf. We also get some implications for the CSM around the progenitor of SN 2009kf and what kind of mass loss should have happened before the explosion of SN 2009kf. Conclusions are given in Section 5.

2 STELLA CODE AND PRE-SUPERNOVA MODELS

STELLA is a one-dimensional multi-group radiation hydrodynamics code (Blinnikov & Bartunov 1993; Blinnikov et al. 1998, 2006). **STELLA** calculates the spectral energy distri-

¹ For the SN classification, see Filippenko (1997) for a review.

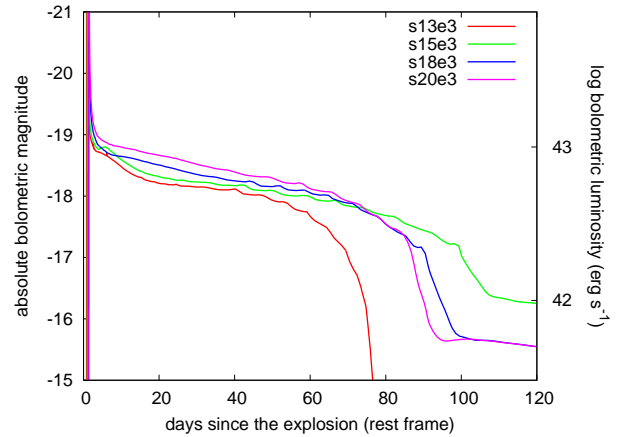
Table 1. List of LC models without CSM

Name	Progenitor	Explosion Energy 10^{51} erg	Radiation Energy ^a 10^{49} erg
s13e3	s13	3	3.0
s15e1	s15	1	1.3
s15e3	s15	3	3.2
s15e5	s15	5	4.9
s18e3	s18	3	3.7
s20e3	s20	3	4.2

^a Radiation energy emitted in 50 days since the explosion.

butions (SEDs) at each time step and we can get multi-color LCs by convolving filter functions to the SEDs. All the calculations are performed by adopting 100 frequency bins from 1 \AA to $5 \times 10^4 \text{ \AA}$. STELLA implicitly treats time-dependent equations of the angular moments of intensity averaged over a frequency bin. Local thermodynamic equilibrium is assumed to determine the ionization levels of materials. For the details of STELLA, see Blinnikov et al. (2006) and the references therein. Comparisons of STELLA with other numerical codes are provided in, e.g., Blinnikov et al. (1998, 2003); Woosley et al. (2007) and analytical models are also compared to the numerical results of STELLA (e.g., Rabinak & Waxman 2011). In this paper, explosions are treated as a thermal bomb by injecting thermal energy just below the mass cut $1.4 M_{\odot}$. We do not follow explosive nucleosynthesis because we focus on the early epochs when the effect of explosive nucleosynthesis on SN LCs is negligible.

We construct pre-SN models by attaching CSM to the progenitor models calculated by Woosley, Heger, & Weaver (2002). As the progenitor models of Woosley, Heger, & Weaver (2002) do not take into account of the extensive mass loss we are interested in, we artificially attach CSM to the outer most layer of the progenitor models. The composition of CSM is solar metallicity and is the same as the surface of the RSG models which we adopt. Compared to the effect of the CSM parameters, the LCs are less affected by the RSG models adopted inside (Section 3.2.6). This justifies our simple way to construct the pre-SN models. Among the pre-SN models shown in Woosley, Heger, & Weaver (2002), we use the solar-metallicity single star models of RSGs; s13, s15, s18, and s20. The ZAMS masses of the models s13, s15, s18, and s20 are $13 M_{\odot}$, $15 M_{\odot}$, $18 M_{\odot}$, and $20 M_{\odot}$, respectively. If they are exploded without CSM, their LCs show a long plateau phase and thus they are Type IIP SN progenitors (Section 3.1). Although we do not follow explosive nucleosynthesis, ^{56}Ni is in the core of the pre-SN models due to the nuclear statistical equilibrium established in the core. However, at the early epochs we are interested in (first ~ 50 days since the explosions), the photons originated from ^{56}Ni decay do not leak from the ejecta so much and contribute little to LCs. According to Figure 2 of Kasen & Woosley (2009), the effect of ^{56}Ni on Type IIP SN LCs appear after ~ 50 days since the explosions and thus our LC models are not applicable from around that epoch. Density structures of the pre-SN models are shown accordingly in the following sections.

**Figure 1.** Bolometric LCs of the SNe from the progenitors without CSM.

3 LIGHT CURVES

In this section, we present the LCs calculated by STELLA. First, we show LCs of the explosions of the progenitors without CSM for references (Section 3.1) and then LCs of the explosions with CSM (Section 3.2).

3.1 Explosions without CSM

In this section, we present the LCs for the progenitors without CSM. The aim of these calculations is to provide references to be compared with LCs with CSM. Note that, as mentioned in Section 2, the LCs shown here are not applicable after ~ 50 days since the explosions because we do not follow explosive nucleosynthesis. Table 1 is the list of the LCs shown in this section. Previous studies also calculated the multicolor LCs of Type IIP SNe from the same progenitor models with different numerical codes (Kasen & Woosley 2009; Dessart, Livne, & Waldman 2010; Dessart & Hillier 2011) and from different progenitor models with the same numerical code (Baklanov, Blinnikov, & Pavlyuk 2005; Tominaga et al. 2009, 2011).

In Figure 1, the bolometric LCs with the same explosion energy (3×10^{51} erg) are presented. When a shock emerges from a stellar surface, a bolometric LC is suddenly brightened due to the shock breakout. Then, the ejecta cools adiabatically. When the outer layer of the ejecta reaches the recombination temperature of hydrogen, the LC becomes flat until the photosphere reaches the bottom of the hydrogen layer (plateau phase). After the plateau phase, the LC follows the decay line of ^{56}Co which existed as ^{56}Ni in the core of the pre-SN model even though we do not calculate the explosive nucleosynthesis (Section 2). Note that our LC models are not applicable after the late epochs of the plateau phase.

The bolometric LCs with the same progenitor (s15) but different explosion energies are shown in the top left panel of Figure 2. In the other panel of Figure 2, we also show the multicolor LCs of each model. Optical LCs are obtained by applying the Bessell *UBVRI* filters (Bessell 1990) and UV LCs are derived by using the near-UV (NUV) imaging filter of the *Galaxy Evolution Explorer* (*GALEX*) satellite whose

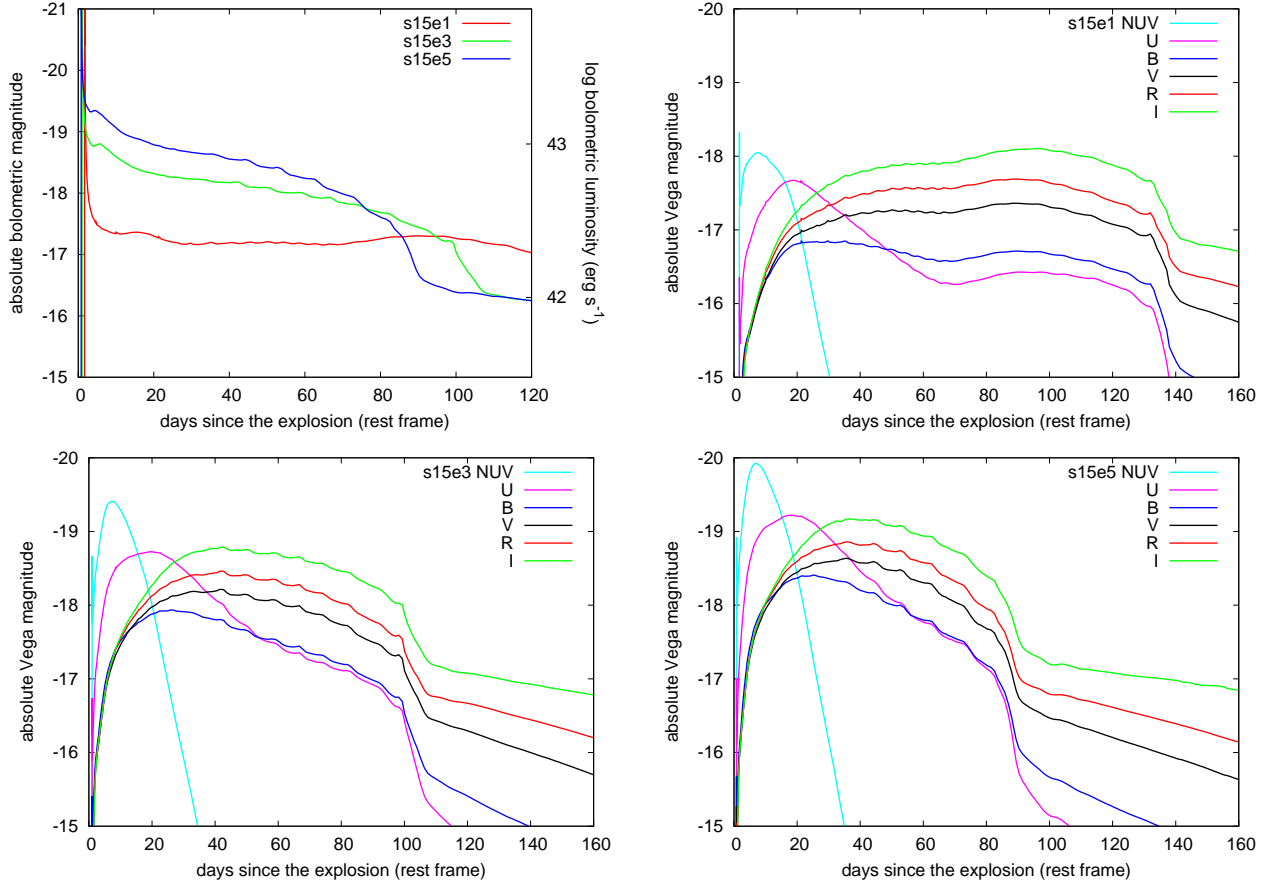


Figure 2. Bolometric (top left) and multicolor (the others) LCs of the SNe from the progenitor s15 without CSM. Models with several explosion energies are shown.

central wavelength is around 2300 Å (Morrissey et al. 2005). After the first brightening due to shock breakout, NUV first become bright because of the adiabatic cooling of the ejecta. Then, LCs become bright in optical as NUV become fainter. This is an important feature of usual Type IIP SNe. They are not bright in UV and optical at the same time. The behavior of the multicolor LCs of the other progenitors is qualitatively the same as the multicolor LCs shown in Figure 2.

3.2 Explosions with CSM

In this section, we investigate the effect of CSM around RSGs on SN LCs. After the explosion of the progenitor, a shock wave propagates inside the progenitor. At these epochs, CSM is not ionized and optically thin. Then, after the shock wave has gone through the surface of the progenitor, a precursor wave appears in the CSM and CSM is ionized. The precursor wave propagates very fast and soon reaches to the surface of CSM. The optical depth (τ_{CSM}) of CSM after the shock wave reached the surface of the progenitor is expressed as

$$\tau_{\text{CSM}} = \int_{R_0}^R \kappa(r)\rho(r)dr \simeq \int_{R_0}^{R_i} \kappa(r)\rho(R_0) \left(\frac{r}{R_0}\right)^{-\alpha} dr, \quad (1)$$

where κ is opacity, ρ is density, R is the CSM radius, R_0 is the radius of the inner edge of CSM where CSM is con-

nected to the progenitor inside, i.e., the radius of the progenitor inside, and R_i is the ionization front in CSM. τ_{CSM} depends on the thickness of the ionized layer because κ above the ionization front is very low ($\kappa \sim 10^{-4} \text{ cm}^2 \text{ g}^{-1}$). In order to estimate a condition in which CSM can affect LCs, we assume that CSM below R_i is fully ionized and the Thomson scattering is the predominant source of opacity ($\kappa(r) = 0.33 \text{ cm}^2 \text{ g}^{-1}$ with solar metallicity). With $R_0 \simeq 5 \times 10^{13} \text{ cm}$ (Figure 3; Section 3.2.6), $R_0 \ll R_i$, and $\alpha \gtrsim 1$, the condition to be $\tau_{\text{CSM}} > 1$ is

$$\rho(R_0) \gtrsim 6 \times 10^{-14} (\alpha - 1) \text{ g cm}^{-3}. \quad (2)$$

Thus, when the density of CSM at the radius where CSM is connected to the progenitor model inside is more than $\sim 10^{-13} \text{ g cm}^{-3}$, CSM becomes optically thick and LCs are expected to be affected by CSM. CSM with mass-loss rates higher than $\sim 10^{-4} M_{\odot} \text{ yr}^{-1}$ satisfies this condition, assuming that the CSM velocity is 10^6 cm s^{-1} (Figure 3).

In the following sections, we also investigate the dependence of LCs on several physical parameters of CSM and progenitors. The parameters of CSM adopted are mass-loss rates [$10^{-1} - 10^{-4} M_{\odot} \text{ yr}^{-1}$], radii of the outer edge of CSM (CSM radii) [$5 \times 10^{14} - 3 \times 10^{15} \text{ cm}$], and density slopes ($\rho \propto r^{-\alpha}$) [$\alpha = 2, 1.5$]. Several progenitor models inside are also adopted [s13, s15, s18, s20]. The density structures of the pre-SN models with CSM are shown accordingly in

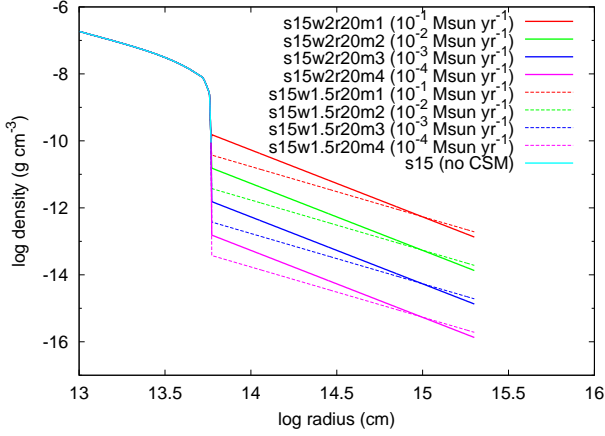


Figure 3. Density structures of the pre-SN models with different mass-loss rates and density slopes. The density structures shown with solid lines have CSM density slope of $\rho \propto r^{-2}$ and those shown with dashed lines have CSM density slope of $\rho \propto r^{-1.5}$. The pre-SN models are constructed by attaching CSM to the progenitor model s15.

the following sections. The model parameters and results are summarized in Tables 2 and 3.

3.2.1 Effect of CSM

Typical bolometric LCs which are affected by CSM are shown in Figure 4 with the bolometric LC from the model without CSM (s15e3). We focus on the model s15w2r20m3e3 to describe the effect of CSM in this section. CSM mainly affects the LCs at the early epochs, roughly until the sudden drop in the LCs which can be seen at around 25 days in the model s15w2r20m3e3 ($10^{-3} M_{\odot} \text{ yr}^{-1}$). At first, LCs have round shapes (until ~ 15 days in s15w2r20m3e3). The round phase is followed by a flat LC which lasts until the sudden drop ($\sim 15 - 25$ days in s15w2r20m3e3). LCs are mainly powered by the interaction of SN ejecta and CSM at these epochs. We call these epochs as an interaction-powered phase (IPP).

The IPP appears in the LCs of the SNe with dense CSM. When the temperature and CSM density are high enough, CSM becomes optically thick and the photosphere locates in CSM. Photosphere during the IPP is in CSM. This can clearly be seen in Figure 5. Looking into the model s15w2r20m3e3, the photospheric velocity is at first 10^6 cm s^{-1} , which is the initial CSM velocity. This is a characteristic feature of the explosions within dense CSM. Then, the photospheric velocity increases due to the acceleration of CSM by the precursor wave. At around ~ 15 days in s15w2r20m3e3, the photosphere reaches the shell between SN ejecta and CSM (Figure 6). Then, the photosphere goes into SN ejecta at ~ 25 days.

All the LCs affected by CSM have round shapes at first (Figure 4). We briefly discuss why the round phase appears. As our models have $\tau_{\text{CSM}} > 1$, photons cannot escape freely from CSM. In addition, our models satisfy the following condition when the shock wave is propagating in CSM:

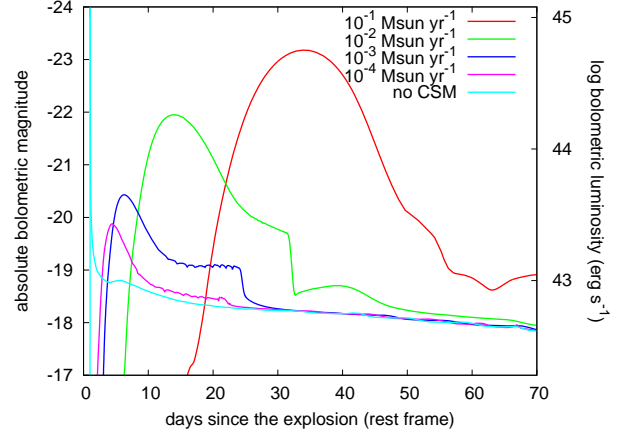


Figure 4. Bolometric LCs of the models with different mass-loss rates. The models shown are s15w2r20m1e3 ($10^{-1} M_{\odot} \text{ yr}^{-1}$), s15w2r20m2e3 ($10^{-2} M_{\odot} \text{ yr}^{-1}$), s15w2r20m3e3 ($10^{-3} M_{\odot} \text{ yr}^{-1}$), and s15w2r20m4e3 ($10^{-4} M_{\odot} \text{ yr}^{-1}$). The bolometric LC of the model s15e3 (no CSM) is also shown for comparison.

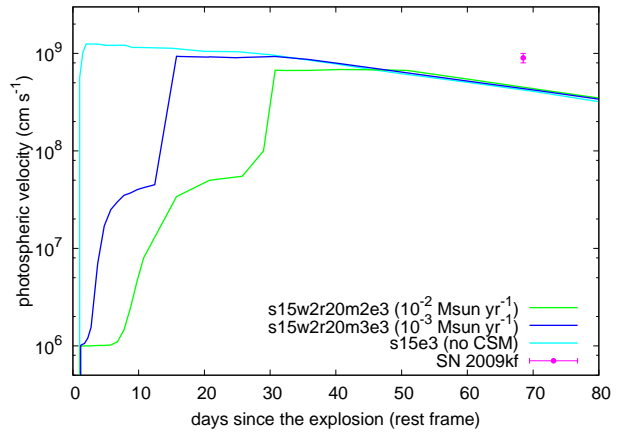


Figure 5. Evolutions of photospheric velocity of the models s15w2r20m2e3, s15w2r20m3e3, and s15e3. The photosphere is defined as the location where the Rosseland optical depth becomes $2/3$. Observed $H\alpha$ line velocity of SN 2009kf is also plotted in the figure. The explosion date of SN 2009kf is set as the same as in Figure 16.

$$\tau_s = \int_{R_s}^R \kappa(r) \rho(r) dr < \frac{c}{v_s}, \quad (3)$$

where R_s is the radius of the shock wave and v_s is the shock velocity. Therefore, photons can diffuse out from the shock wave and a precursor wave propagates ahead of the shock wave (see the left panels of Figure 6). As the shock velocity is typically $\simeq 10^9 \text{ cm s}^{-1}$ when the shock wave reaches R_0 , c/v_s is typically ~ 10 at that time. Thus, photons in the models with

$$\rho(R_0) \lesssim 6 \times 10^{-13} \text{ g cm}^{-3} \quad (4)$$

start to leak photons from the shock wave just after the shock wave reaches R_0 . The other models satisfy Equation 3 when the shock wave propagates in CSM because the deceleration of the shock wave makes c/v_s higher and the

Table 2. List of LC models with CSM

Name	Progenitor	Explosion Energy 10^{51} erg	Mass-Loss Rate ^a $M_{\odot} \text{ yr}^{-1}$	Radius 10^{15} cm	Density Slope α ($\rho \propto r^{-\alpha}$)	CSM Mass M_{\odot}	Radiation Energy ^b 10^{49} erg
s13w2r20m2e3	s13	3	10^{-2}	2	2	0.65	20
s15w2r05m2e3	s15	3	10^{-2}	0.5	2	0.15	9.8
s15w2r05m3e3	s15	3	10^{-3}	0.5	2	0.015	3.8
s15w2r10m2e3	s15	3	10^{-2}	1	2	0.31	13
s15w2r10m3e3	s15	3	10^{-3}	1	2	0.031	4.2
s15w2r20m2e1	s15	1	10^{-2}	2	2	0.65	5.6
s15w2r20m1e3	s15	3	10^{-1}	2	2	6.5	75
s15w1.5r20m1e3	s15	3	–	2	1.5	6.5	80
s15w2r20m2e3	s15	3	10^{-2}	2	2	0.65	19
s15w1.5r20m2e3	s15	3	–	2	1.5	0.65	15
s15w2r20m2e5	s15	5	10^{-2}	2	2	0.65	32
s15w2r20m2e7	s15	7	10^{-2}	2	2	0.65	45
s15w2r20m3e3	s15	3	10^{-3}	2	2	0.065	5.0
s15w1.5r20m3e3	s15	3	–	2	1.5	0.065	4.8
s15w2r20m4e3	s15	3	10^{-4}	2	2	0.0065	3.4
s15w1.5r20m4e3	s15	3	–	2	1.5	0.0065	3.4
s15w2r30m2e3	s15	3	10^{-2}	3	2	0.98	23
s15w2r30m3e3	s15	3	10^{-3}	3	2	0.098	5.6
s18w2r20m2e3	s18	3	10^{-2}	2	2	0.65	17
s20w2r20m2e3	s20	3	10^{-2}	2	2	0.65	17

^a Derived by assuming a constant CSM velocity 10^6 cm s^{-1} .

^b Radiation energy emitted in 50 days since the explosion.

Table 3. Properties of SNe from s15 at some selected epochs

Epoch ^d (days)	L_{bol}^a ($10^{43} \text{ erg s}^{-1}$)				v_{ph}^b (km s^{-1})				T_{BB}^c (10^3 K)			
	10	20	30	40	10	20	30	40	10	20	30	40
s15e1	0.27	0.26	0.23	0.23	6900	6500	5900	5000	15	9.8	7.9	7.0
s15e3	0.84	0.65	0.60	0.57	12000	11000	9500	7800	16	9.8	8.0	7.1
s15e5	1.3	1.0	0.90	0.81	15000	13000	12000	9200	15	9.9	8.0	7.1
s15e7	1.7	1.4	1.2	1.0	17000	16000	13000	10000	16	9.9	8.1	7.1
s15w2r05m2e3	1.1	0.63	0.73	0.57	8100	8300	8300	7800	15	9.0	7.7	7.2
s15w2r05m3e3	0.82	0.69	0.61	0.56	10000	10000	9400	7800	13	9.6	8.0	7.2
s15w2r10m2e3	22	0.78	0.73	0.64	950	7800	7500	7600	42	9.1	7.9	7.2
s15w2r10m3e3	1.5	0.72	0.61	0.56	9800	9800	9400	7800	14	9.1	8.0	7.2
s15w2r20m2e1	0.81	3.2	1.2	0.67	14	86	130	150	15	21	14	10
s15w2r20m1e3	0.049	1.9	47	36	10	15	410	1200	6.0	13	37	32
s15w1.5r20m1e3	0.064	1.5	45	46	10	12	400	1400	6.0	12	36	34
s15w2r20m2e3	9.1	8.4	2.5	0.92	65	500	7200	6800	29	23	11	7.2
s15w1.5r20m2e3	5.0	7.9	3.0	0.64	43	290	6300	5600	23	25	16	7.5
s15w2r20m2e5	29	7.6	1.2	1.1	670	1000	8900	9000	39	20	7.9	7.3
s15w2r20m2e7	58	8.1	1.7	1.3	570	11000	11000	10000	42	16	8.2	7.4
s15w2r20m3e3	2.1	1.3	0.62	0.57	420	9400	9200	7800	18	9.5	8.0	7.2
s15w1.5r20m3e3	2.1	1.5	0.62	0.36	270	9200	9200	7800	18	9.8	8.1	7.2
s15w2r20m4e3	0.96	0.74	0.61	0.57	11000	10000	9400	7800	16	10	8.1	7.1
s15w1.5r20m4e3	0.90	0.77	0.61	0.56	11000	10000	9500	7800	17	11	8.1	7.2
s15w2r30m2e3	2.8	15	4.4	2.5	21	210	300	330	20	26	16	10
s15w2r30m3e3	3.5	1.3	1.1	0.61	30	9400	9100	8000	21	9.8	8.7	7.3

^a Bolometric luminosity.

^b Photospheric velocity. Photosphere is where the Rosseland optical depth is 2/3.

^c Color temperature at photosphere. Photosphere is where the Rosseland optical depth is 2/3.

^d Epoch since the explosion.

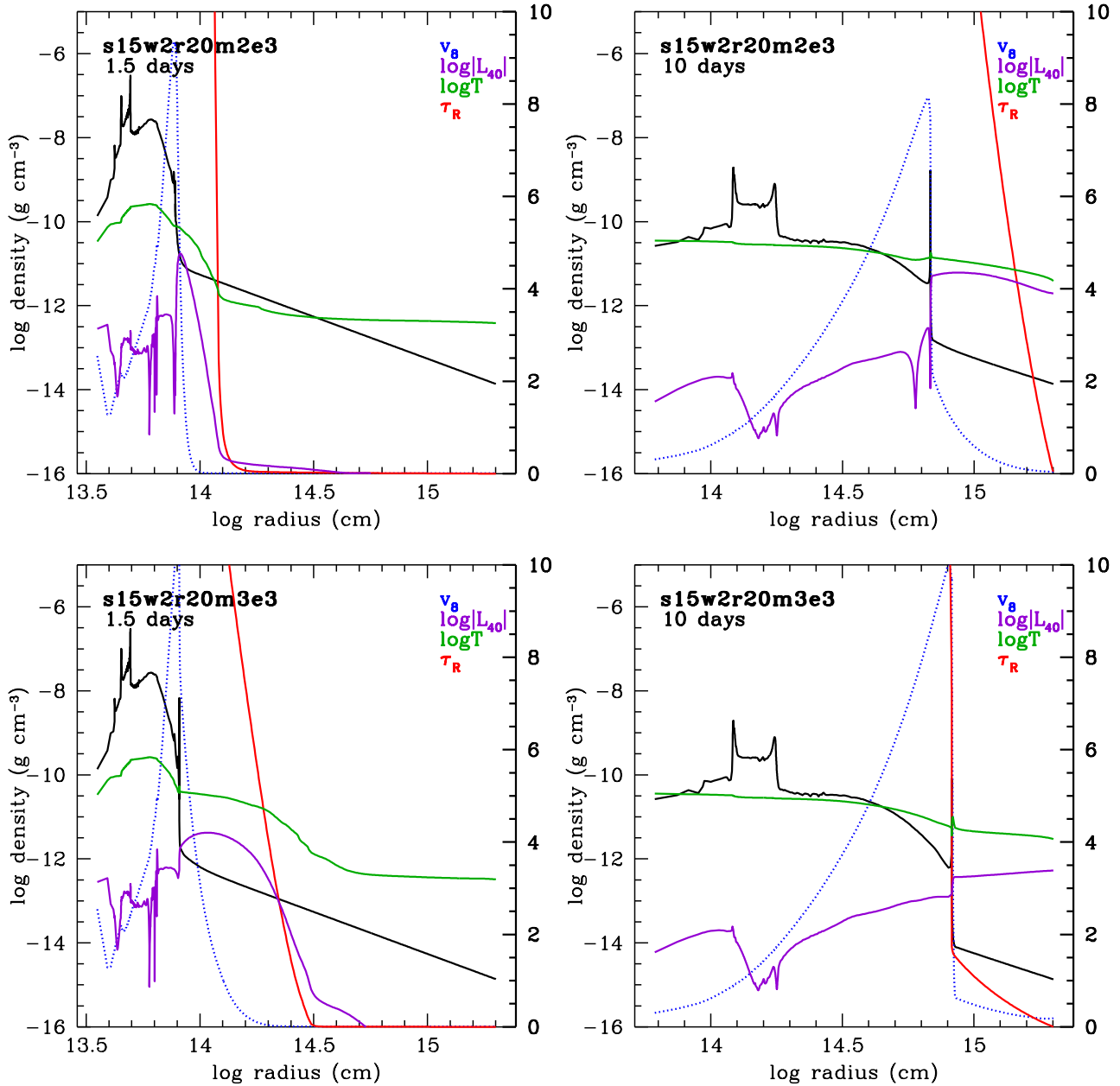


Figure 6. Physical structures of the models s15w2r20m2e3 and s15w2r20m3e3 at two epochs. The epochs are the days since the explosion. Black lines show the density structure (left y -axis). Blue lines are the velocity scaled by 10^8 cm s^{-1} (right y -axis), purple lines are the logarithm of the absolute value of luminosity scaled by 10^{40} erg s^{-1} (right y -axis), green lines are the logarithm of the temperature in Kelvin (right y -axis), and red lines are Rosseland optical depth measured from the outside (right y -axis).

propagation of the shock wave reduces τ_s . Once Equation 3 is satisfied, photons start to leak out from the shock wave and this phenomenon is usually observed as shock breakout. However, since there is dense CSM at the time of shock breakout, photons diffuse out in CSM and shock breakout signal become longer compared with the explosions without CSM (see also Falk & Arnett 1973, 1977).

In addition, SN ejecta is decelerated by the dense CSM. Dense CSM is massive and it has the density structure $\rho \propto r^{-2}$ if it is from steady mass loss. Thus, the shock wave between the SN ejecta and CSM is decelerated and

kinetic energy of the SN ejecta is converted to thermal energy which is released as radiation energy. As a result, SNe with dense CSM emit more photons and become brighter than those without dense CSM. For further discussion, see, e.g., Chevalier & Irwin (2011). Comparing radiation energy emitted during early epochs (Tables 1 and 2), it is clear that the effect of the SN ejecta deceleration is dominant radiation source during the IPP. In other words, the round phase is not just due to the elongation of the shock breakout signal seen in the models without CSM (e.g. s15e3).

The difference in the rising times and durations of the

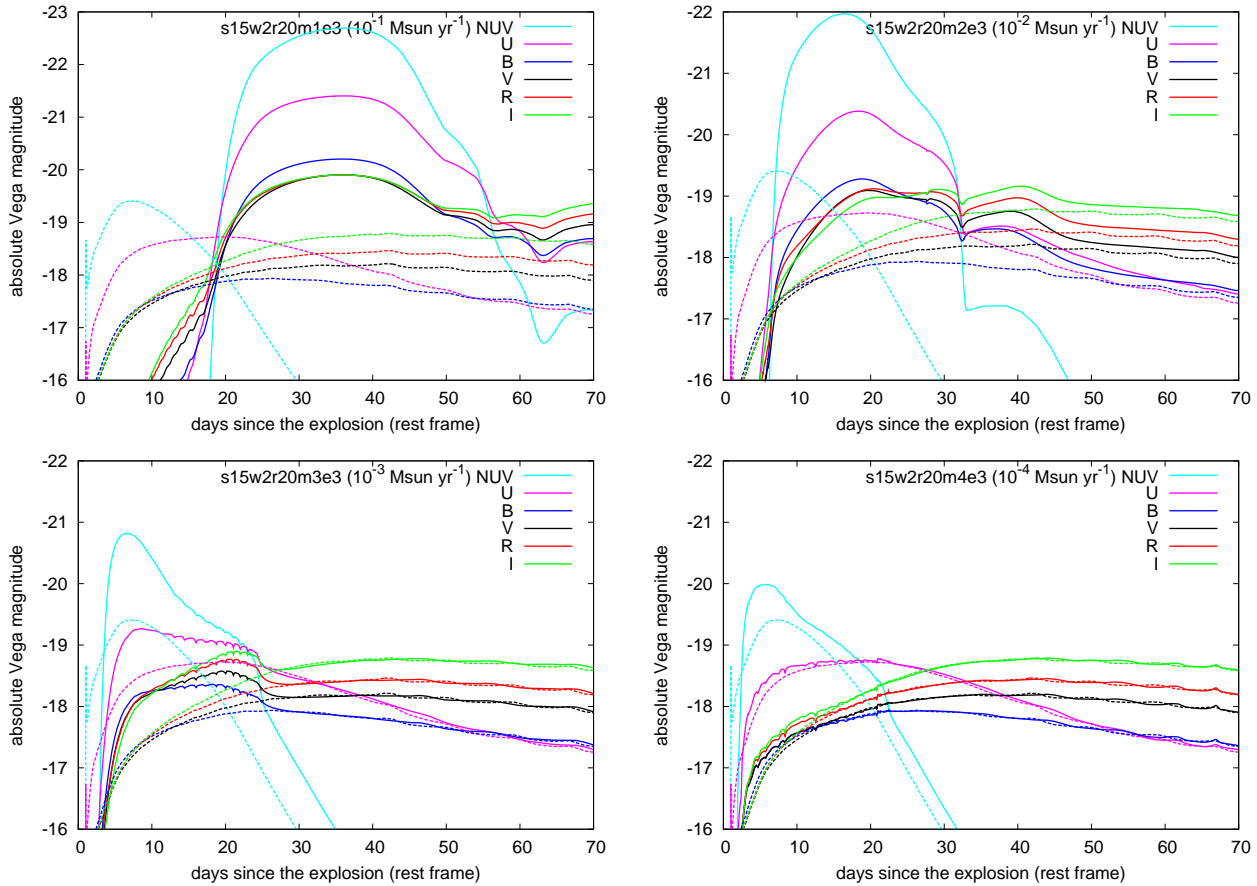


Figure 7. Multicolor LCs of the models with different mass-loss rates (solid lines). The dashed lines are the multicolor LCs of the model s15e3 for comparison. LCs of the same color are from the same filter. Note that top left panel has different y -axis range from the other panels.

round LCs during the IPP comes from the difference in diffusion timescales of CSM (Figure 4). The models with higher mass-loss rates have denser CSM and thus longer diffusion timescales. This difference due to diffusion timescales can be clearly seen in Figure 6. The upper panels and the lower panels represent the same epoch of the explosion with different CSM densities, i.e., different CSM diffusion timescales. As is indicated by the temperature waves in CSM which are pushed by the photon diffusion, photons in CSM with shorter diffusion timescales diffuse out more quickly into CSM. Therefore, the rising times and the durations of the round phase in the IPP are shorter for the models with the smaller CSM diffusion timescales. Those differences are also discussed in Falk & Arnett (1973, 1977).

The round LC in the IPP is followed by the flat LC which lasts until the sudden drop of the LC (between around 15 days and 25 days in s15w2r20m3e3). During this flat phase, the photosphere locates at the dense shell between SN ejecta and CSM. The photospheric velocity does not change so much during the flat phase (Figure 5). After CSM above the dense shell have become optically thin, the photosphere remains at the dense shell until the temperature and density of the shell becomes low enough to be optically thin.

One of the clear characteristics of the LCs with CSM is the sudden drop in the LCs. The time of this sudden

drop corresponds to the time when the dense shell becomes optically thin and the photosphere proceeds inward to SN ejecta. This can also be seen in the photospheric velocity evolution (Figure 5). The brightness can drop as low as the LC without CSM because now the photons are emitted from SN ejecta and the physical conditions are the same as those of SNe without dense CSM. However, the brightness is still slightly more luminous than the LC without CSM for several days after the sudden drop. This could be because of the extra-heating due to shock and/or deceleration of SN ejecta by CSM which makes the adiabatic cooling of SN ejecta less efficient.

There are many differences between our models (RSG + CSM) and RSGs with extended envelopes. First of all, it is difficult to have RSGs extended to $\sim 10^{15}$ cm (e.g., Woosley, Heger, & Weaver 2002). What is more, density and temperature in RSGs are much higher in RSG envelopes than in CSM. This does not allow the shock wave in RSGs to satisfy Equation 3 until the shock wave reaches the surface of RSGs. In other words, the shock wave does not break out until it reaches near the surface. On the contrary, in our models, Equation 3 is satisfied inside CSM and the precursor wave propagates ahead of the shock wave. In addition, the kinetic energy of the SN ejecta efficiently converted to radiation energy because of the deceleration of the SN ejecta

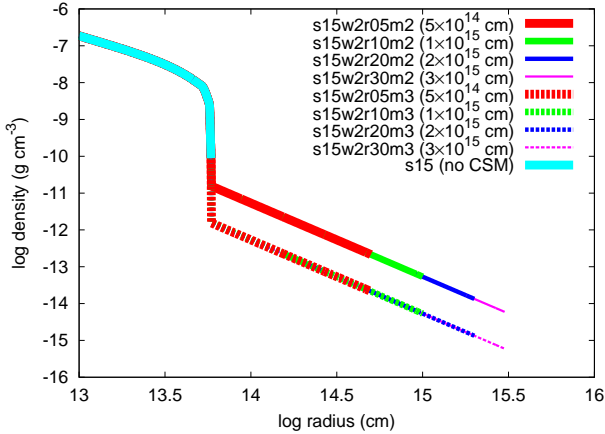


Figure 8. Density structures of the pre-SN models with different radii. Models with solid lines have the mass-loss rate $10^{-2} M_{\odot} \text{ yr}^{-1}$ and those with dashed lines have $10^{-3} M_{\odot} \text{ yr}^{-1}$. The pre-SN models are constructed by attaching CSM to the progenitor model s15.

by the dense CSM. This precursor wave due to the shock breakout in CSM and an additional heating source causes the IPP phase.

3.2.2 Dependence on Mass-Loss Rate

In this section, we show the effect of mass-loss rates on LCs. We adopt the mass-loss rates of 10^{-1} , 10^{-2} , 10^{-3} , and $10^{-4} M_{\odot} \text{ yr}^{-1}$ (the corresponding model names are s15w2r20m1, s15w2r20m2, s15w2r20m3, and s15w2r20m4, respectively). For the case of $10^{-1} M_{\odot} \text{ yr}^{-1}$, CSM mass is $6.5 M_{\odot}$ and the sum of the mass of RSG inside and CSM exceeds the ZAMS mass of the progenitor. This is unrealistic but we show the results just to see the effect of CSM. Every CSM in the models is optically thick (Equation 2; Figure 3). These mass-loss rates are derived by assuming that the CSM velocity is 10^6 cm s^{-1} . However, the escape velocity of the surface of s15 is $7.6 \times 10^6 \text{ cm s}^{-1}$. This means that the CSM velocity can be higher than 10^6 cm s^{-1} at least at the late stages of the evolution of the progenitor and thus the actual mass-loss rate for a given CSM density could be higher than the values we show. The flow from the progenitor may not be even steady. However, we assume that CSM results from the steady flow from the progenitor with the velocity 10^6 cm s^{-1} for simplicity because the CSM velocity has little effect on LCs. To see the effect of the mass-loss rates on the LCs, we fix the radius of CSM to $2 \times 10^{15} \text{ cm}$ and the density slope to $\rho \propto r^{-2}$ in this section. Also, the explosion energy and the progenitor of the SNe are fixed to $3 \times 10^{51} \text{ erg}$ and s15. The density structures of the progenitors with CSM are shown in Figure 3.

Figure 4 shows the bolometric LCs of the SNe with different mass-loss rates. Since the diffusion timescale of CSM becomes larger for denser CSM, rising times and durations of round phases in LCs are longer for the models with higher mass-loss rates. The maximum luminosity of the LCs becomes larger as CSM becomes denser. This is because the shock wave is more decelerated by CSM due to the more massive CSM, i.e., more kinetic energy is converted to the

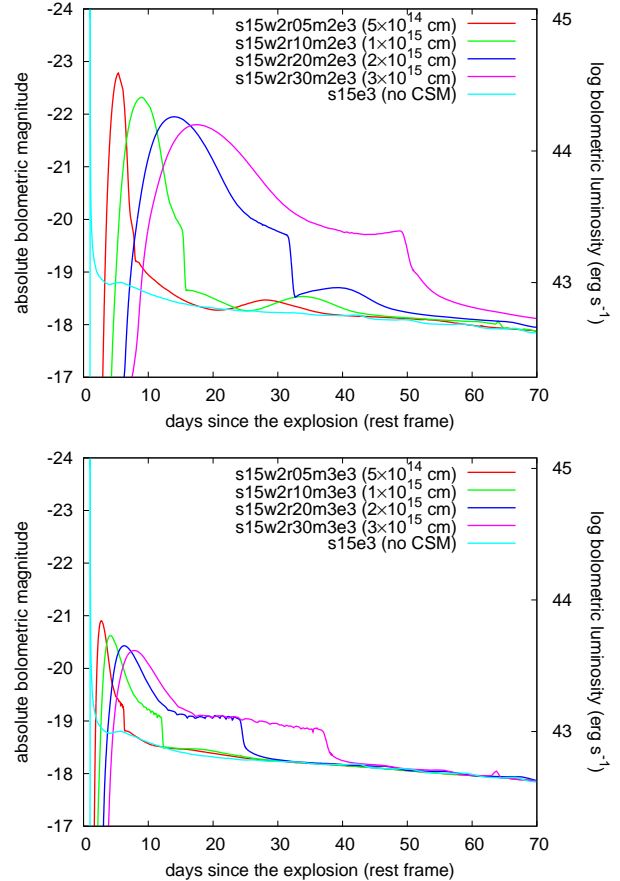


Figure 9. Bolometric LCs of the models with different CSM radii. The top panel shows the LCs from the models with the mass-loss rate $10^{-2} M_{\odot} \text{ yr}^{-1}$ and the bottom panel shows those with $10^{-3} M_{\odot} \text{ yr}^{-1}$. The bolometric LC of the model s15e3 is also shown for comparison.

thermal energy and thus radiation energy. The radiation energies of the models are summarized in Table 2.

The multicolor LCs of the models in this section are shown in Figure 7. Each LC is plotted with the multicolor LCs of no CSM model s15e3. It is clear that the LCs during the IPP become bright especially in short wavelengths because of high temperatures at the photosphere.

3.2.3 Dependence on Radius

In this section, the effect of the CSM radius on LCs is investigated. To see the effect of the CSM radius, we fix the following parameters; the explosion energy ($3 \times 10^{51} \text{ erg}$), the density slope ($\alpha = 2$), and the progenitor inside (s15). We try two mass-loss rates, $10^{-2} M_{\odot} \text{ yr}^{-1}$ and $10^{-3} M_{\odot} \text{ yr}^{-1}$. We adopt four CSM radii to see the effect, i.e., $5 \times 10^{14} \text{ cm}$ (s15w2r05m2 and s15w2r05m3), $1 \times 10^{15} \text{ cm}$ (s15w2r10m2 and s15w2r10m3), $2 \times 10^{15} \text{ cm}$ (s15w2r20m2 and s15w2r20m3), and $3 \times 10^{15} \text{ cm}$ (s15w2r30m2 and s15w2r30m3). With the constant CSM velocity 10^6 cm s^{-1} , the mass loss in the models lasts 16 years, 32 years, 64 years, and 96 years, respectively. The density structures of the pre-SN models are shown in Figure 8.

Figure 9 shows the bolometric LCs of the models with

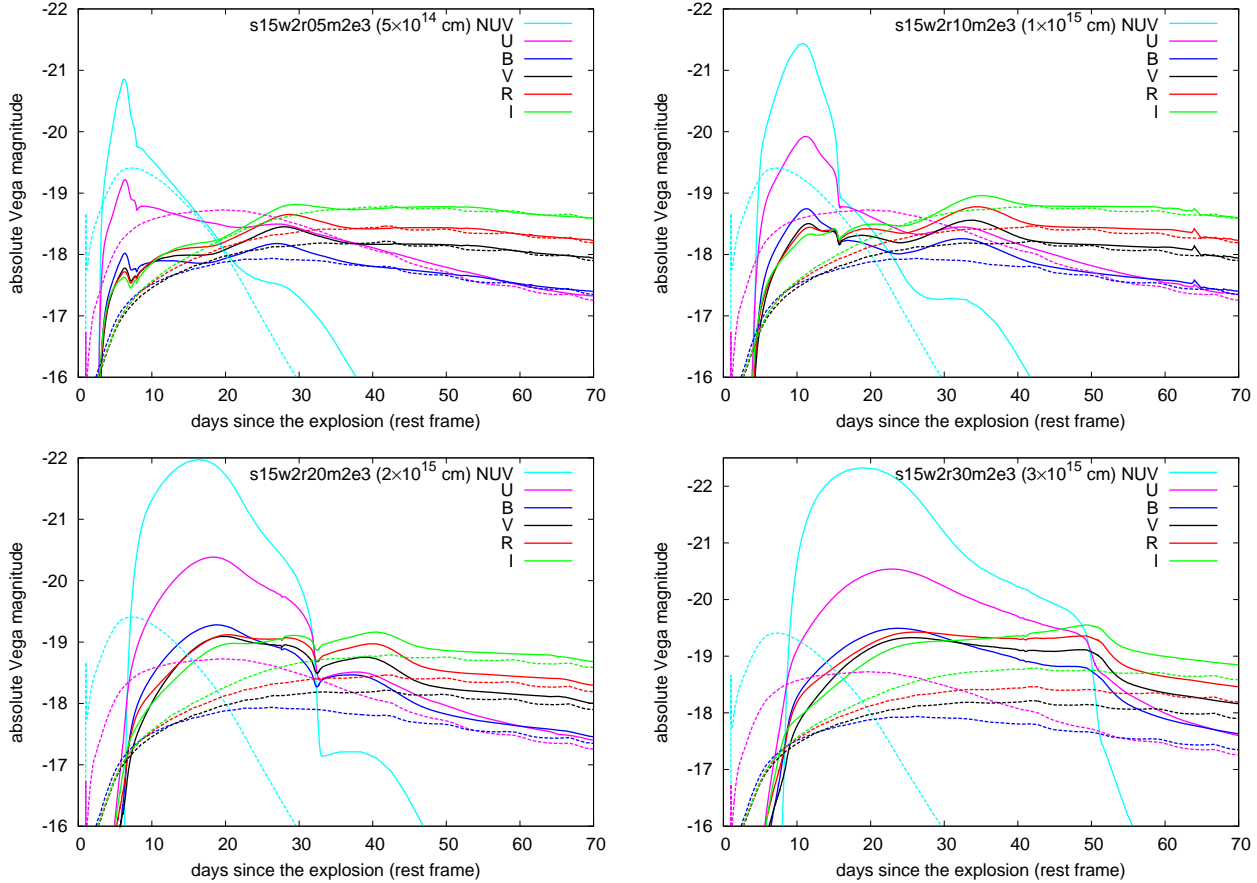


Figure 10. Multicolor LCs of the models with different radii (solid lines). The dashed lines are the multicolor LCs of the model s15e3 for comparison. LCs of the same color are from the same filter. Note that the scale of y -axis in the right bottom panel (s15w2r30m2e3) is different from those in the other panels.

different CSM radii. The durations of the round phases in the IPP are longer for the models with the larger CSM radius. This is because the diffusion times of the LCs are longer for the models with the larger CSM radius. On the other hand, the maximum luminosities of the round phases decrease as the CSM radius increases. As the explosion energy and the density structure are similar in each model, the radiation energy released by the shock interaction is also close to each other (see Table 2 for the radiation energy emitted in each model). Therefore, the difference in the maximum luminosities is caused by the difference in the diffusion timescales. Even if the same energy is released in the same timescale, photons are more scattered and distribute more uniformly in CSM for models with longer diffusion timescales. Thus, the luminosity, i.e., radiation energy released from the CSM surface in a unit time, becomes lower for the models with larger CSM radii. The flat phase of IPP is also longer for the models with the larger radius.

The multicolor LCs of the models with $10^{-2} M_{\odot} \text{ yr}^{-1}$ are shown in Figure 10. Although s15w2r05m2e3 has the brightest peak bolometric luminosity among the models, the NUV and *UBVRI* band LCs of the model are the faintest. This is because the more compact CSM is, the hotter CSM becomes. The photosphere of the model s15w2r05m2e3 is too hot during the IPP to emit the radiation in the NUV and

UBVRI bands. The SEDs of the models at the bolometric peak are shown in Figure 11.

3.2.4 Dependence on Density Slope

The CSM density slope of $\rho \propto r^{-2}$ results from the steady flow from the central progenitor. However, if mass loss is not steady, the density slope does not necessarily have the density structure $\rho \propto r^{-2}$ and can be shallower ($\alpha < 2$) or steeper ($\alpha > 2$). For example, the shallower density slope of CSM is suggested in the modeling of the spectra of Type IIIn SNe (e.g., Chugai et al. 2004). We calculate the LCs with the slope $\alpha = 1.5$. As we are fixing the CSM velocity, mass-loss rates should change with time to have the density slope $\alpha = 1.5$. The CSM radius (2×10^{15} cm), the explosion energy (3×10^{51} erg), and the progenitor inside (s15) are fixed in this section. To see the effect of density slopes, we calculate the models with the same CSM masses as the models with the density slope $\alpha = 2$, i.e., $6.5 M_{\odot}$ (s15w1.5r20m1), $0.65 M_{\odot}$ (s15w1.5r20m2), $0.065 M_{\odot}$ (s15w1.5r20m3), $0.0065 M_{\odot}$ (s15w1.5r20m4). The density structures of the pre-SN models are shown in Figure 3.

Figure 12 shows the bolometric LCs. The dependence on CSM mass in the case $\alpha = 1.5$ is similar to that of the case $\alpha = 2$. Looking into the bolometric LCs with the same

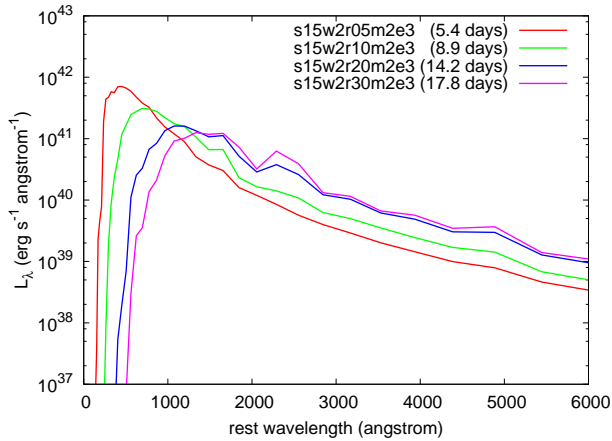


Figure 11. SEDs of the models with different radii at the epoch of the maximum bolometric luminosity. The mass-loss rate of the models is $10^{-2} M_{\odot} \text{ yr}^{-1}$.

CSM mass, the LCs with $\alpha = 1.5$ are fainter until around the bolometric peak and then become brighter. This is because in the case of $\alpha = 1.5$, CSM is denser outside and thinner inside compared to the case of $\alpha = 2$ (Figure 3). Since the kinetic energy is more efficiently converted to the radiation energy with denser CSM, LCs from shallower CSM become brighter at later epochs. Although the luminosity of LCs is affected by density slopes, the durations of the round phase and the epochs of the sudden drop in the cases of $\alpha = 1.5$ are similar to the cases of $\alpha = 2$ and are not strongly affected by density slopes.

The multicolor LCs are similar to those shown in Figure 7. The NUV absolute Vega magnitudes become as bright as -22.8 mag, -21.7 mag, -20.7 mag, and -20.0 mag for the models s15w1.5r20m1e3, s15w1.5r20m2e3, s15w1.5r20m3e3, and s15w1.5r20m4e3, respectively.

3.2.5 Dependence on Explosion Energy

In this section, we look into the effect of the explosion energy on LCs. As the higher explosion energy leads to the higher kinetic energy of the SN ejecta, the luminosities of the LCs during the IPP are expected to be higher with the higher explosion energies. The fixed parameters in this section are the mass-loss rate ($10^{-2} M_{\odot} \text{ yr}^{-1}$), the CSM radius (2×10^{15} cm), the density slope ($\alpha = 2$), and the progenitor (s15). The explosion energies we adopt are 1×10^{51} erg (s15w2r20m2e1), 3×10^{51} erg (s15w2r20m2e3), 5×10^{51} erg (s15w2r20m2e5), and 7×10^{51} erg (s15w2r20m2e7). The density structure of the models in this section is the same as that of the model s15w2r20m2 (Figure 3).

Figure 13 is the bolometric LCs of the explosions with different explosion energies. As expected, the LCs become brighter with higher explosion energies. Since the shock propagates faster in a higher energy model, the model has a shorter rising time and a shorter duration. However, the LCs are less sensitive to explosion energies than mass-loss rates and radii. This is because the CSM parameters have direct effect on diffusion timescales, while the explosion energy determines the strength of the shock wave where photons are emitted.

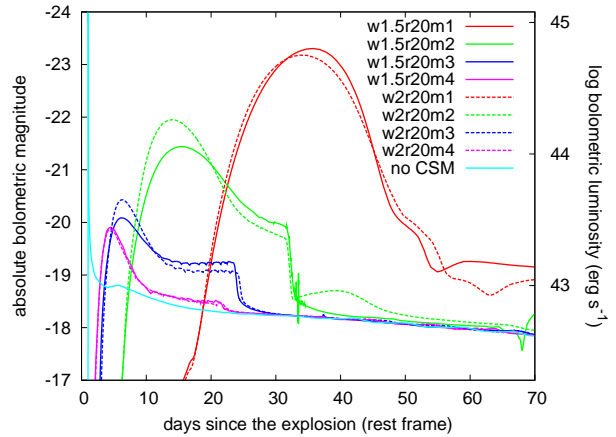


Figure 12. Bolometric LCs of the models with different CSM density slopes and mass-loss rates. The bolometric LCs shown with solid lines have CSM density slope of $\rho \propto r^{-1.5}$ and those shown with dashed lines have CSM density slope of $\rho \propto r^{-2}$. 's15' in the model names are omitted in the figure. The bolometric LC of the model s15e3 (no CSM) is also shown for comparison.

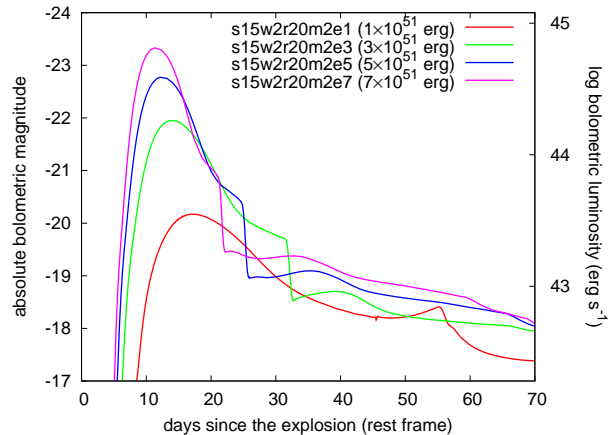


Figure 13. Bolometric LCs from the model s15w2r20m2 with different explosion energies.

The multicolor LCs of all the models shown in this section are similar to those of the model s15w2r20m2e3 in Figure 7 with different rising times, durations, and brightness. The rising times and durations are the same as those of the corresponding bolometric LCs and the NUV absolute Vega magnitudes become as bright as -21.0 mag, -22.4 mag, and -22.8 mag for the models s15w2r20m2e1, s15w2r20m2e5, and s15w2r20m2e7, respectively.

3.2.6 Dependence on Progenitor

In the previous sections, the progenitor model inside CSM is fixed to s15. As LCs during the IPP are powered by the shock interaction of SN ejecta and CSM, the effect on LCs due to the difference in progenitors (RSGs) inside is expected to be small. To confirm this, we calculate the LCs of the models which have different progenitors but the same CSM parameters. The CSM parameters fixed are the mass-

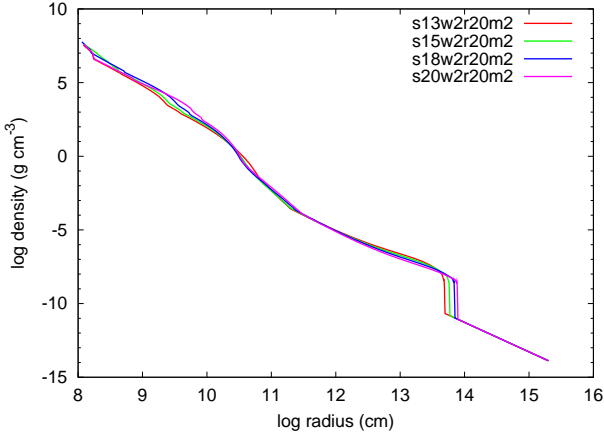


Figure 14. Density structures of the pre-SN models with different progenitor models inside.

loss rate ($10^{-2} M_{\odot} \text{ yr}^{-1}$), the CSM radius ($2 \times 10^{15} \text{ cm}$), and the density slope ($\alpha = 2$). The explosion energy is also fixed to $3 \times 10^{51} \text{ erg}$. We use Type IIP SN progenitors s13 (s13w2r20m2), s15 (s15w2r20m2), s18 (s18w2r20m2), and s20 (s20w2r20m2) to see the effect. Figure 14 shows the density structures of the models. We note that the CSM density structures of the models are slightly different from each other because the radius where CSM is connected to the central progenitor is different depending on the pre-SN models.

Figure 15 shows the LCs with different progenitors. Roughly speaking, the LCs are similar to each other because all the progenitors are RSGs and properties of progenitors, like radii or density structures, are not dramatically different from each other. There are slight differences in the maximum luminosities and the epochs of the sudden drop in the LCs due to the slight difference in those properties of progenitors.

The multicolor LCs are also similar to those of the model s15w2r20m2e3 (Figure 7). The NUV absolute Vega magnitudes become as bright as -22.0 mag , -21.8 mag , and -21.9 mag for the models s13w2r20m2e3, s18w2r20m2e3, and s20w2r20m2e3, respectively.

4 DISCUSSION

In this section, we compare our LCs obtained in the previous section to that of UV-bright Type IIP SN 2009kf whose LC is suggested to be affected by dense CSM (Botticella et al. 2010). We show that the LC of SN 2009kf is actually reproduced by the LC models with dense CSM and we get constraints on the state of the CSM around the progenitor of SN 2009kf at the pre-SN stage.

4.1 Observations of SN 2009kf and Light Curve Modeling

SN 2009kf was discovered by Pan-STARRS 1 survey and observed by *GALEX* using the NUV filter (Botticella et al. 2010). The observations of SN 2009kf by *GALEX* revealed its distinguishing features: SN 2009kf was continued to be bright in NUV for more than 10 days and it was also bright

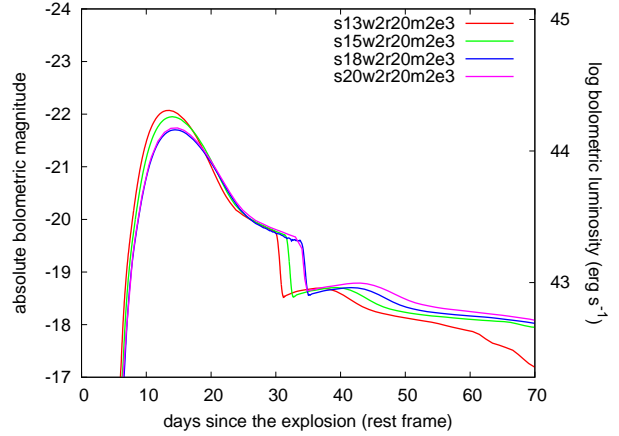


Figure 15. Bolometric LCs of the models with different progenitors inside.

in the optical bands during the same period. This feature is difficult to be explained by Type IIP SN models without dense CSM. This is because, after the shock breakout, the UV LCs of Type IIP SNe without dense CSM decline rapidly due to the adiabatic cooling of the ejecta and the absorptions by iron group elements. Therefore, the optical brightness of Type IIP SNe without dense CSM increases as the ejecta cools down with the decreasing UV brightness (Figure 2). Utrobin, Chugai, & Botticella (2010) try to model the LC of SN 2009kf without dense CSM and they find that large explosion energy ($2 \times 10^{52} \text{ erg}$) is required to obtain the LC of SN 2009kf.

One big uncertainty is in the extinction of SN 2009kf. Although the galactic extinction is negligible ($E(B - V) = 0.009 \text{ mag}$; Schlegel, Finkbeiner, & Davis 1998), the host extinction is estimated as $E(B - V) = 0.32 \pm 0.5 \text{ mag}$ (Botticella et al. 2010). The large uncertainty in the host extinction makes it difficult to estimate its absolute NUV magnitudes. The redshift of the host galaxy is 0.182 ± 0.002 (Botticella et al. 2010).

In Figure 16, we show a comparison of the model s15w2r20m2e3 with the LCs of SN 2009kf. The SED derived at each time step in *STELLA* is reddened with the host extinction assuming the extinction law of Cardelli, Clayton, & Mathis (1989) and then shifted to the redshift 0.182 by using the standard Λ CDM cosmology with $H_0 = 70 \text{ km s}^{-1} \text{ Mpc}^{-1}$, $\Omega_M = 0.3$, and $\Omega_{\Lambda} = 0.7$. The host extinction we apply here is $E(B - V) = 0.22 \text{ mag}$. The left panel of Figure 16 shows the LCs in the first 60 days since the explosion in the observer frame. The solid lines are the model LCs and the points are the observations by Botticella et al. (2010). The epochs of observations are shifted arbitrarily. There is little contribution of ^{56}Ni produced by explosive nucleosynthesis on LCs at these epochs. The model LCs are in good agreement with the observations. Especially, the characteristic observational feature that the NUV LC and the optical LCs are bright at the same epochs is well-reproduced, as well as the NUV brightness. In the right panel of Figure 16, the LCs at the later epochs are also shown. Since the explosive nucleosynthesis (amount of ^{56}Ni produced), the progenitor model inside (mass of hydrogen layer), and the degree of mixing of ^{56}Ni in H-rich layer mainly affect the

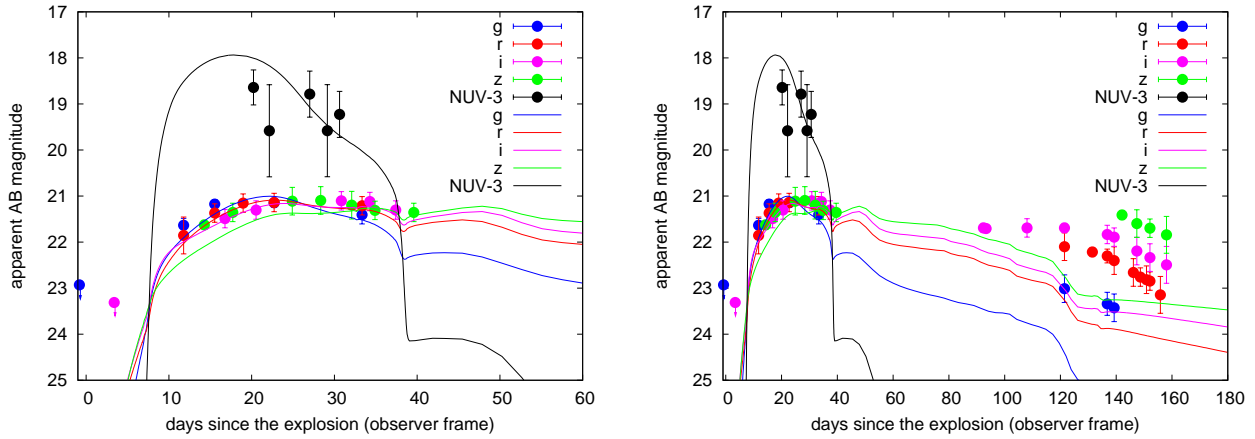


Figure 16. Comparison of the model LCs from s15w2r20m2e3 with the observed LCs of SN 2009kf. Each point is observed LCs and the solid lines are the model LCs shifted to the observer frame. The epochs of the observation points are shifted arbitrarily. The model LCs are obtained by reddening the SEDs obtained by numerical calculations with the host extinction of $E(B - V) = 0.22$ mag and then adopting the redshift 0.182. Magnitudes of NUV are shifted by 3 magnitudes in this figure.

LCs at the epochs after the IPP (e.g., Kasen & Woosley 2009; Dessart, Livne, & Waldman 2010; Dessart & Hillier 2011; Bersten, Benvenuto, & Hamuy 2011), modeling this part of the LCs is out of our scope. Especially, if we include such an effect, photosphere is expected to be located outer than our model and photospheric velocity becomes faster. The model shown in Figure 16 has the explosion energy of 3×10^{51} erg and the evolution of the photospheric velocity is shown in Figure 5 with the observed $H\alpha$ line velocity. Although our model LCs have slower photospheric velocity, it is expected to increase as is mentioned above. Large amount of ^{56}Ni production is expected from the long plateau phase after the IPP. In addition, the observational facts that the bolometric luminosity at the plateau phase is very high and the $H\alpha$ line velocities of SN 2009kf are very large also indicate large explosion energy of SN 2009kf. Note that the LCs during the IPP are not sensitive to the central progenitor model (Section 3.2.6) and progenitor models other than s15 can also work.

4.2 CSM around the Progenitor of SN 2009kf

Given that the only observational data we are able to compare with our model LCs are those during the IPP and that the difference in progenitors inside (RSGs) does not have much effect on LCs during the IPP (Section 3.2.6; Figure 15), it is difficult to constrain the ZAMS mass of the progenitor of SN 2009kf. However, as we show in Section 3.2, the LCs of the IPP is strongly affected by the CSM parameters and we can get constraints on them. In this section, we try to make constraints on the CSM around the progenitor of SN 2009kf at the pre-SN stage.

First, as discussed in Section 3.2.1, the mass-loss rate of the progenitor should be larger than $\sim 10^{-4} M_{\odot} \text{ yr}^{-1}$ to see the effect of the CSM on LCs. The duration of the UV-bright phase of SN 2009kf indicates that the CSM radius is larger than $\sim 1 \times 10^{15}$ cm (Section 3.2.3; Figure 9). Although a model with low explosion energy and a small CSM radius can result in LCs with a duration similar to that of SN 2009kf, the high bolometric luminosity and the large line velocities of

SN 2009kf are difficult to be reproduced by such low-energy explosion.

The absolute NUV magnitude of the UV-bright phase is required to make further constraints on CSM. However, due to the uncertainty in the host extinction, it is difficult to get the absolute NUV magnitude of SN 2009kf. Therefore, what we can confidently conclude is that SN 2009kf has a LC naturally explained by the CSM interaction (long-lasting UV brightness during the period when it is also bright in optical) and the mass-loss rate of its progenitor should be higher than $10^{-4} M_{\odot} \text{ yr}^{-1}$ just before or at the time of the explosion to see such effect on the LCs, assuming that the CSM velocity is 10^6 cm s^{-1} . The CSM radius which is larger than $\sim 1 \times 10^{15}$ cm is inferred from the duration and brightness of the NUV LC. If the host extinction is assumed to be $E(B - V) = 0.22$ mag, the multicolor LC model of the IPP shown in Figure 16, which has the CSM with the mass-loss rate $10^{-2} M_{\odot} \text{ yr}^{-1}$ and the radius 2×10^{15} cm, is consistent with the UV-bright phase of SN 2009kf. We note that the density slope of the CSM does not have much effect on the duration of the IPP as shown in Section 3.2.4 and we cannot constrain the density slope with our model.

4.3 Progenitor of SN 2009kf and Its Extensive Mass Loss

The high bolometric luminosity at the plateau phase and very high line velocities of SN 2009kf imply that SN 2009kf had a high explosion energy. In addition, the long plateau phase indicates that the amount of ^{56}Ni produced by the explosive nucleosynthesis is large. Since Type IIP SNe from higher ZAMS mass progenitors tend to be more energetic and produce more ^{56}Ni (e.g., Hamuy 2003; Utrobin & Chugai 2009), the progenitor of SN 2009kf is indicated to be one of the most massive RSGs and may come from the high mass end of RSGs. Therefore, it is indicated that the most massive RSGs can have a very high mass-loss rate and that such extensive mass loss can occur just before the explosions of the massive RSGs.

Not only LCs but also spectra can be affected by the

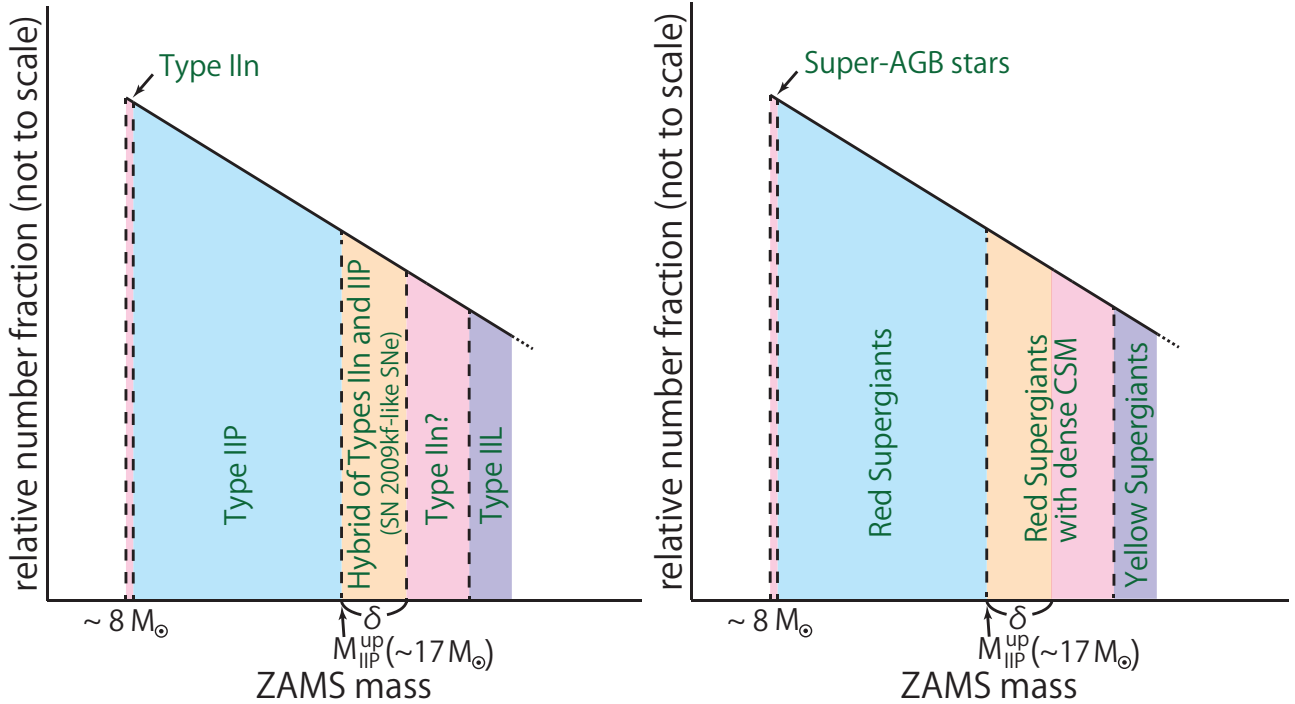


Figure 17. *Left:* Possible relation between ZAMS mass and SN types. We set the maximum ZAMS mass of Type IIP SNe as $M_{\text{IIP}}^{\text{up}}$, which is observationally suggested to be $\sim 17 M_{\odot}$ (Smartt et al. 2009). Dense CSM may be left at the time of SN explosions at a ZAMS mass range above $M_{\text{IIP}}^{\text{up}}$. If there is enough CSM, the SNe can be Type IIn. On the other hand, there can be a small ZAMS mass range from $M_{\text{IIP}}^{\text{up}}$ to $M_{\text{IIP}}^{\text{up}} + \delta$ (with small δ), in which there is not enough CSM for the SN to continue to be Type IIn and the SN can be a hybrid of Type IIP and Type IIn. SN 2009kf and SN 1987C are possible candidates for such a hybrid SN. The number fraction of SNe (y -axis) is determined by an initial mass function. *Right:* The same as left but plotted with progenitor stars. The explosion of RSGs without dense CSM is expected from $\sim 8 M_{\odot}$ to $M_{\text{IIP}}^{\text{up}}$. RSGs explode within dense CSM above $M_{\text{IIP}}^{\text{up}}$. A yellow supergiant is observationally found to be the progenitor of Type IIL SN 2009kr. The ZAMS mass of the yellow supergiant is estimated as $\sim 18 - 24 M_{\odot}$ (Elias-Rosa et al. 2010) and $15^{+5}_{-4} M_{\odot}$ (Fraser et al. 2010), which are consistent with our picture.

existence of dense CSM. During the IPP phase of SNe from RSGs with dense CSM, photosphere is located in CSM and very narrow P-Cygni profiles, which are similar to those of Type IIn SNe, are expected to be observed (Figure 5). Then, after the IPP, their spectra shift to those of Type IIP SNe. In other words, SN 2009kf-like SNe can be a hybrid type of Type IIn and Type IIP (Figure 17). If extensive mass loss of massive RSGs happen just before their explosions, CSM mass and/or radius can be so small that the interaction of dense CSM and SN ejecta ends in early epochs. Then, the corresponding SN may be observed as a hybrid of Type IIn and Type IIP and SN 2009kf might be classified as Type IIn if early spectra were taken. If there is large and/or massive enough CSM or a shell exists that is created long before the explosion due to extensive mass loss, the SNe may be purely Type IIn and may not show the feature of Type IIP SNe (Figure 17). Our prediction that the early spectra of SN 2009kf-like SNe have narrow lines is what clearly differs from theoretical models suggested by Utrobin, Chugai, & Botticella (2010).

While no spectra of SN 2009kf were taken during the IPP, SN 1987C are suggested to have shown such transition of the spectra from a Type IIn SN-like blue spectrum with narrow hydrogen emission lines to Type IIP SN spectra (Schlegel & Kirshner 1998). The Type IIn SN-like spectrum of SN 1987C is taken at 52 days since its discovery when

SN 1987C could have been approaching to the end of the IPP. At 79 days after the discovery, the spectrum showed the P-Cygni profile of hydrogen lines and the line velocity of $\text{H}\alpha$ was high (6800 km s^{-1}). Although SN 1987C was not observed by UV, this transition of the spectra could indicate that SN 1987C may be another sample of an explosion of a RSG within a dense CSM. The high $\text{H}\alpha$ line velocities indicates that the progenitor of SN 1987C was a massive RSG. Such early observations of SN spectra are important to find other candidate SNe which are the hybrid of Type IIn and Type IIP.

Although we show a possible evidence for the existence of extensive mass loss of a massive RSG, the mechanism is still uncertain. A candidate for the mechanism to achieve this kind of mass loss is the pulsations of RSGs (Yoon & Cantiello 2010; Heger et al. 1997; Li & Gong 1994). As shown by Yoon & Cantiello (2010), this mechanism can potentially make a mass-loss rate of a RSG as high as $10^{-2} M_{\odot} \text{ yr}^{-1}$. What is more, for the RSGs with ZAMS masses around $17 M_{\odot}$, the pulsations just before the explosion and the CSM can potentially remain dense until the time of the explosion. Coincidentally, the minimum ZAMS mass to cause the pulsations obtained by Yoon & Cantiello (2010) is roughly the same as the maximum ZAMS mass of Type IIP SN progenitors indicated by observations ($17 M_{\odot}$, Smartt et al. 2009). Such extensive mass loss in massive

Type IIP SN progenitors may suppress the upper limit on the ZAMS mass of Type IIP SN progenitors because such mass loss can take the whole hydrogen layer out of the progenitors. Mass loss due to nuclear flash may also be a driving force of the extensive mass loss (Weaver & Woosley 1979; Dessart, Livne, & Waldman 2010).

Rareness of UV-bright Type IIP SNe similar to SN 2009kf can be interpreted as a relatively small ZAMS mass range of this event. For example, no Type IIP SNe observed with *Swift* satellite show the long term UV-brightening which is expected by CSM interaction (Brown et al. 2009). The rareness of UV-bright Type IIP SNe also support that they may come from the high mass end of Type IIP SN progenitors (Figure 17). Note, however, that the rareness can also be interpreted in different ways. For example, it is possible that RSGs generally have extensive mass loss (due to, e.g., nuclear flashes) but it usually occurs long before their explosions and the mass range of the progenitors which experience extensive mass loss just before the explosions is small. Future early spectral and UV observations of Type IIP SNe are required to get more samples of SN 2009kf-like SNe so that we can make constraint on the mass range of SN 2009kf-like SNe and on the driving force of such extensive mass loss. Observations of nebular phase spectra are also important for determining the ZAMS mass of such SNe (e.g., Dessart, Livne, & Waldman 2010).

5 CONCLUSIONS

(i) We show that the existence of dense CSM affects LCs of explosions of RSGs. This is because (1) shock breakout signals are elongated by CSM and (2) SN ejecta is decelerated by CSM. In particular, because of the deceleration, kinetic energy of SN ejecta is converted to thermal energy which is emitted as radiation and SNe can be brighter than usual. The LC becomes bright in UV as well as in optical. In addition, the photospheric velocity of early epochs is very low because the photosphere is located in CSM at early epochs. The most influential parameters of CSM are mass-loss rates and radii. The mass-loss rate should be higher than $\sim 10^{-4} M_{\odot} \text{ yr}^{-1}$ to show the effect of CSM. Higher mass-loss rates and/or larger radii lead to longer diffusion timescales of CSM and thus, longer durations and rising times of the LCs powered by the interaction. Density slopes and explosion energies also slightly change LCs. The difference in Type IIP SN progenitor (RSG) models inside CSM are not so sensitive to LCs. (Section 3)

(ii) The LCs of Type IIP SN 2009kf, which were bright in UV as well as in optical in early phases (Botticella et al. 2010), can be explained by the pre-SN models with dense CSM. The mass-loss rate of the progenitor of SN 2009kf should be higher than $10^{-4} M_{\odot} \text{ yr}^{-1}$. The CSM radius is expected to be larger than $\sim 1 \times 10^{15}$ cm. The explosion energy of SN 2009kf is likely to be very high because of its high bolometric luminosity at the plateau phase and its high line velocities. The long duration of the plateau phase of SN 2009kf implies that the large amount of ^{56}Ni is produced by the explosion.

(iii) The high explosion energy and the large amount of ^{56}Ni produced indicate that the progenitor of SN 2009kf is a massive RSG. Our results show that massive RSGs are likely

to experience extensive mass loss exceeding $10^{-4} M_{\odot} \text{ yr}^{-1}$ just before their explosions. The explosions of such massive RSGs with extensive mass loss will be SN 2009kf-like SNe. Their spectra show the transition from Type II_n SN-like spectra to Type IIP SN spectra which is observed in SN 1987C (Schlegel & Kirshner 1998). The existence of such SNe indicates that there is some mechanism to enhance mass loss of massive RSGs, like pulsations discussed by Yoon & Cantiello (2010) or nuclear flashes suggested by Weaver & Woosley (1979). Such a mechanism may reduce the maximum ZAMS mass of Type IIP SN progenitors predicted by single star evolution modeling ($\sim 25M_{\odot}$; e.g., Heger et al. 2003) as low as the observationally implicated value ($\sim 17M_{\odot}$; e.g., Smartt et al. 2009) (Figure 17).

(iv) Future early spectral and UV observations of SNe will find other SNe similar to SN 2009kf and provide LCs with long time coverage and spectra at the IPP. Large samples and detailed observations of SN 2009kf-like SNe can reveal the mass-loss mechanism of RSGs as well as the nature of SN 2009kf-like SNe.

ACKNOWLEDGMENTS

We thank the referee for his/her comments which improved the text very much. We also thank Christopher S. Kochanek for his comment. All the numerical calculations were carried out on the general-purpose PC farm at Center for Computational Astrophysics, CfCA, of National Astronomical Observatory of Japan. T.M. would like to thank Naoki Yoshida and Keiichi Maeda for their supports for his visits to University of Texas at Austin and Max Planck Institute for Astrophysics. The work of S.B., P.B., and E.S. in Russia is supported partly by the grants RFBR 10-02-00249, 10-02-01398 by "Scientific School" grants 3458.2010.2, 3899.2010.2, by contract with Agency for Science and Innovation No. 02.740.11.0250, SNSF grant No. IZ73Z0-128180/1 under the program SCOPES. This research is supported in part by a grant from the Hayakawa Satio Fund awarded by the Astronomical Society of Japan. This research has also been supported in part by World Premier International Research Center Initiative, MEXT, Japan.

REFERENCES

- Andrews J. E., et al., 2010, ApJ, 715, 541
- Arcavi I., et al., 2010, ApJ, 721, 777
- Baklanov P. V., Blinnikov S. I., Pavlyuk N. N., 2005, AstL, 31, 429
- Bersten M. C., Benvenuto O., Hamuy M., 2011, ApJ, 729, 61
- Bessell M. S., 1990, PASP, 102, 1181
- Blinnikov S. I., Bartunov O. S., 1993, A&A, 273, 106
- Blinnikov S., Chugai N., Lundqvist P., Nadyozhin D., Woosley S., Sorokina E., 2003, fthp.conf, 23
- Blinnikov S. I., Eastman R., Bartunov O. S., Popolitov V. A., Woosley S. E., 1998, ApJ, 496, 454
- Blinnikov S. I., Röpke F. K., Sorokina E. I., Gieseler M., Reinecke M., Travaglio C., Hillebrandt W., Stritzinger M., 2006, A&A, 453, 229

- Blinnikov S. I., Sorokina E. I., 2010, arXiv, arXiv:1009.4353
 Boissier S., Prantzos N., 2009, *A&A*, 503, 137
 Botticella M. T., et al., 2010, *ApJ*, 717, L52
 Boyer M. L., et al., 2010, *A&A*, 518, L142
 Brown P. J., et al., 2009, *AJ*, 137, 4517
 Cardelli J. A., Clayton G. C., Mathis J. S., 1989, *ApJ*, 345, 245
 Chevalier R. A., Irwin C. M., 2011, *ApJ*, 729, L6
 Chugai N. N., et al., 2004, *MNRAS*, 352, 1213
 Dessart L., Hillier D. J., 2011, *MNRAS*, 410, 1739
 Dessart L., Hillier D. J., Gezari S., Basa S., Matheson T., 2009, *MNRAS*, 394, 21
 Dessart L., Livne E., Waldman R., 2010, *MNRAS*, 405, 2113
 Dessart L., Livne E., Waldman R., 2010, *MNRAS*, 408, 827
 Elias-Rosa N., et al., 2010, *ApJ*, 714, L254
 Falk S. W., Arnett W. D., 1973, *ApJ*, 180, L65
 Falk S. W., Arnett W. D., 1977, *ApJS*, 33, 515
 Filippenko A. V., 1997, *ARA&A*, 35, 309
 Fraser M., et al., 2010, *ApJ*, 714, L280
 Georgy C., Meynet G., Walder R., Folini D., Maeder A., 2009, *A&A*, 502, 611
 Hamuy M., 2003, *ApJ*, 582, 905
 Heger A., Fryer C. L., Woosley S. E., Langer N., Hartmann D. H., 2003, *ApJ*, 591, 288
 Heger A., Jeannin L., Langer N., Baraffe I., 1997, *A&A*, 327, 224
 Kasen D., Woosley S. E., 2009, *ApJ*, 703, 2205
 Li Y., Gong Z. G., 1994, *A&A*, 289, 449
 Metzger B. D., 2010, *MNRAS*, 409, 284
 Morrissey P., et al., 2005, *ApJ*, 619, L7
 Pozzo M., Meikle W. P. S., Fassia A., Geballe T., Lundqvist P., Chugai N. N., Sollerman J., 2004, *MNRAS*, 352, 457
 Rabinak I., Waxman E., 2011, *ApJ*, 728, 63
 Schlegel D. J., Finkbeiner D. P., Davis M., 1998, *ApJ*, 500, 525
 Schlegel E. M., Kirshner R. P., 1998, *NewA*, 3, 125
 Smartt S. J., 2009, *ARA&A*, 47, 63
 Smartt S. J., Eldridge J. J., Crockett R. M., Maund J. R., 2009, *MNRAS*, 395, 1409
 Smith N., Hinkle K. H., Ryde N., 2009, *AJ*, 137, 3558
 Smith N., Li W., Filippenko A. V., Chornock R., 2011, 412, 1522
 Tominaga N., Blinnikov S., Baklanov P., Morokuma T., Nomoto K., Suzuki T., 2009, *ApJ*, 705, L10
 Tominaga N., Morokuma T., Blinnikov S. I., Baklanov P., Sorokina E. I., Nomoto K., 2011, *ApJS*, 193, 20
 Utrobin V. P., Chugai N. N., 2009, *A&A*, 506, 829
 Utrobin V. P., Chugai N. N., Botticella M. T., 2010, *ApJ*, 723, L89
 van Marle A. J., Smith N., Owocki S. P., van Veelen B., 2010, *MNRAS*, 407, 2305
 Weaver T. A., Woosley S. E., 1979, *BAAS*, 11, 724
 Woosley S. E., Blinnikov S., Heger A., 2007, *Natur*, 450, 390
 Woosley S. E., Heger A., Weaver T. A., 2002, *RvMP*, 74, 1015
 Woosley S. E., Kasen D., Blinnikov S., Sorokina E., 2007, *ApJ*, 662, 487
 Yoon S.-C., Cantiello M., 2010, *ApJ*, 717, L62

